DOI: 10.1039/c6ra18833h

RSC Advances

PAPER

View Article Online
View Journal | View Issue

Cite this: *RSC Adv.*, 2016, **6**, 87888

Synthesis and porous h-BN 3D architectures for effective humidity and gas sensors†

Chandkiram Gautam,*[ab] Chandra Sekhar Tiwary,*[a] Leonardo D. Machado,[c] Sujin Jose,[ad] Sehmus Ozden,[a] Santoshkumar Biradar,[a] Douglas S. Galvao,[c] Rakesh K. Sonker,[e] B. C. Yadav,[e] Robert Vajtai[a] and P. M. Ajayan*[a]

Received 25th July 2016
Accepted 26th August 2016

DOI: 10.1039/c6ra18833h

www.rsc.org/advances

3D (three dimensional) architectures synthesised using an easily scalable solid state method which results in an interconnected network of porous h-BN sheets with boron trioxide are reported in this study. The boron trioxide acts as a nucleating agent for the formation of laterally large nanosheets of h-BN with a low density and increases the specific surface area. The stable form shows improved mechanical properties (experimentally and using MD simulation) and serves as a suitable material for humidity and liquefied petroleum gas (LPG) sensor applications. The sensor shows stability for up to several months without losing its sensitivity.

1. Introduction

Three-dimensional (3D) graphene architecture have been synthesized using different novel approaches.[1–3] Therefore, it is anticipated that developing 3D h-BN architectures will increase their significance in various applications.[4–6] Hexagonal boron nitride (h-BN) nanosheets (also known as white graphene), possess a number of significant properties such as high oxidation resistance, good chemical stability, optical luminescence, thermal conductivity and electrical insulating properties.[7–10] Previously, it has been reported that graphene and monolayer boron nitride were used as strain tunable nanosensors.[11–13] Recently, Mulpur *et al.* reported sensing applications on MoS_2/WS_2/BN-silver thin-film hybrid architectures.[14] More recently, Liu *et al.* reported highly porous BN nanosheets for superior adsorption of pharmaceutical molecules.[15] However, they also reported unique synthesis and applications of highly crumpled and porous h-BN nanosheet membranes for adsorbents and superior trapping emulsified oils and organic molecules.[16,17] Humidity sensors are being extensively studied in recent times as they find applications in biomedical, meteorological studies, food quality control and storage, domestic electric appliances (such as drying machines and microwave ovens), air conditioning systems and several other feedback control systems.[18–25] Aoki *et al.* have worked on the characterization of boron carbon nitride film and its application as humidity sensor which works at high temperature at 730 °C.[26] Yu *et al.* has developed a humidity sensor using a single Au-decorated boron nitride nanotube; the humidity sensing response was found as 85% at room temperature.[27] Soltani *et al.* worked on the hexagonal boron nitride thin films and reported the influence of humidity on its electrical properties.[28]

Apart from these applications, researchers are working towards the fabrication of gas sensors of portable size for practical applications ranging from identification of toxic gasses to monitoring of manufacturing process.[29,30] As the liquefied petroleum gas (LPG) and other high-risk gasses are widely being used in several industrial and domestic applications,[31,32] the need for high performance and effective gas sensors with suitable sensing materials has increased. 2D (two-dimensional) materials have long been of interest in the perspectives due to their distinct optical, electrical and catalytic properties.[33] The two elements contain materials (*e.g.* A and B in AB sheet) are an attractive subject for the study and their sensing properties are superior to those of single phase materials.[34] Porous nanostructures of 2-D materials can be used as building blocks for the construction of highly sensitive sensing nano-devices.[35] Mesoporous materials increase the impingement rate of molecules, *i.e.*, the adsorption rate of gasses on the surface of the sensing materials. The decrease in the response and recovery times of the sensor due to high adsorption and desorption rates of the target gasses and hence the fast sensing device may be

[a]*Department of Materials Science and Nano Engineering, Rice University, Houston, Texas, USA. E-mail: gautam_ceramic@yahoo.com; ajayan@rice.edu; cst.iisc@gmail.com*

[b]*Department of Physics, University of Lucknow, Lucknow – 226007, Uttar Pradesh, India*

[c]*Instituto de Física "Gleb Wataghin", Universidade Estadual de Campinas, CP 6165, 13083-970 Campinas, Brazil*

[d]*Department of Physics, Kamaraj University, Madurai – 625021, Tamilnadu, India*

[e]*Department of Applied Physics, School of Physical Sciences, Babasaheb Bhimrao Ambedkar University, Lucknow – 226025, Uttar Pradesh, India*

† Electronic supplementary information (ESI) available. See DOI: 10.1039/c6ra18833h

constructed using the porous nonmaterial. BN/Pd composite films were chosen by Ghosh *et al.* to build a reliable liquid petroleum gas sensor with the sensitivity of 13.2%, sensing response 1.15 and operable at 187 °C.[36] However, the sensing properties of 3D h-BN nanostructures are yet to be reported. Therefore, in this current study, we are focusing on the synthesis of low-density porous 3D h-BN using a simple bottom-up approach of the solid-state method. The synthesized porous structures demonstrated to be structurally stable, with low density, and controllable porosity. Besides the mechanical stability, they showed excellent humidity and LPG gas sensing capabilities.

2. Experimental methods

The synthesis process of 3D porous h-BN architecture is described as below: 7.372 g of B_2O_3 and 2.628 g of h-BN (molar ratio of 50 : 50) were mixed in acetone media for 6 h. The thoroughly mixed powder was dried and transferred into a porcelain crucible and kept into a programmable electric furnace to sinter at 1000 °C with heating rate of 5 °C m^{-1} for 3 h soaking time in Ar gas atmosphere. Eventually, white porous h-BN powder was produced. Pellets of the sintered powders were prepared using a pressure load of 3.5 ton for further measurements. X-ray diffraction (XRD) patterns of the samples were collected using a Rigaku D/Max Ultima II. The elemental analysis of different chemical compositions were investigated with the help of X-ray photoelectron spectroscopy (XPS, PHI Quantera XPS) on a PHI–5000C ESCA system with Al KR X-ray as an excitation source. Thermogravimetry (TGA) and differential thermal analysis (DTA) were carried out on a SDTQ-600 thermal analyzer from room temperature to 400 °C at a heating rate of 5 °C m^{-1} under Ar flow. The surface areas and average pore diameter distribution of the samples were measured using a Quantachrome Autosorb-3b Brunauer–Emmett–Teller (BET) surface analyzer. The morphology of the samples was observed using FEI Quanta 400 scanning electron microscope. The transmission electron microscope (TEM) images and diffraction patterns were taken using JEOL 2100 field emission gun transmission electron microscope. Instron universal testing machine was employed to obtain the compressive stress *versus* strain curve from the samples at room temperature. For humidity and LPG sensing measurements, the synthesized porous h-BN films having thickness ~9 μm were deposited on corning glass substrate. The details of experimental setup and measurement methods were described in previous reports.[37]

3. Results and discussion

3.1. XRD analysis

The X-ray powder diffraction (XRD) was used to study the structure of the final product. The XRD pattern (Fig. 1a) indicates that the sample has the h-BN hexagonal structure. There are two major broad diffraction peaks at 26.36° and 41.26° corresponding to planes (002) and (100). Further, as we increased the concentration of B_2O_3, the peak broadening occurs (Fig. S1-ESI†).

3.2. FTIR analysis

In order to understand the bond formation, FTIR analysis was performed. FTIR spectrum (Fig. 1b) shows the peak at wave number 1410 cm^{-1} associated with the stretching vibration of B–N.[38] The peak located at 1190 cm^{-1} could be assigned to the bending vibration of B–O–H. The strong IR absorption peak at 3180 cm^{-1} attributed to the stretching vibration of O–H. The FTIR pattern for the higher concentration of B_2O_3 ($90B_2O_3$: 10BN) is shown in Fig. S2-ESI.† The B–N bands were found to be slightly shifted towards the lower wave number side that is at 1370 cm^{-1}, while the bending vibration of B–O–H remains nearly unaltered.

3.3. X-ray photoelectron spectroscopic and BET analysis

The X-ray photoelectron spectroscopy (XPS) was used to investigate the chemical states of B and N elements. Fig. S3 (ESI†) shows the typical B1s and N1s spectra. Their corresponding binding energies were observed at 194.21 and 398.4 eV respectively.[39,40] In the inset of the Fig. S3,† right side, the shoulder peak at 190.5 eV in the B1s spectrum is attributed to B–O bond, which could have resulted from the precursor.[41,42] The surface area is increasing with increasing the concentration of h-BN with boron trioxide (Fig. 1d). The values of the BET surface area and BET pore size of the synthesized h-BN doped samples lie in the range from 0.92–2.5 m^2 g^{-1} and 0.189 to 3.25 nm, respectively (Table 1). Only the evaporation process is responsible for the generation of porous structure and the enhancement of surface area during the sintering processes at elevated temperature.[43,44] Further, a graph has been plotted on the basis of BET results between the volume absorbed and relative pressure for different samples which are sintered at 1000 °C for 3 h soaking time (Fig. 1e). From the graph it is observed that the maximum volume has been absorbed for the sample $50B_2O_3$: 50BN due to its highly porous nature. The percentage of porosity of the sample was calculated using the density results and was found to be ~36.4%.

3.4. Scanning and transmission electron microscopic analysis

The scanning electron microscopy (SEM) and transmission electron microscopy (TEM) were used to study the morphology of the samples. Typical 3D morphology of the prepared BN sample was shown by the SEM image (Fig. 2a). Fig. 2b–d, enlarged view of the images, clearly reveal the porous BN 3D architecture with interconnected network. Fig. 2d shows the well interconnected BN sheets of the order of submicron (0.98 μm). A schematic of the interconnect structure of BN sheets is shown in Fig. 2e. For better understanding, the pores are marked by the red colored arrows while the BN sheets are marked by yellow colored arrows as shown in these images. The TEM images shown in Fig. 2f–i are in agreement with the observations from SEM (Fig. 2a–d). Both SEM and TEM images

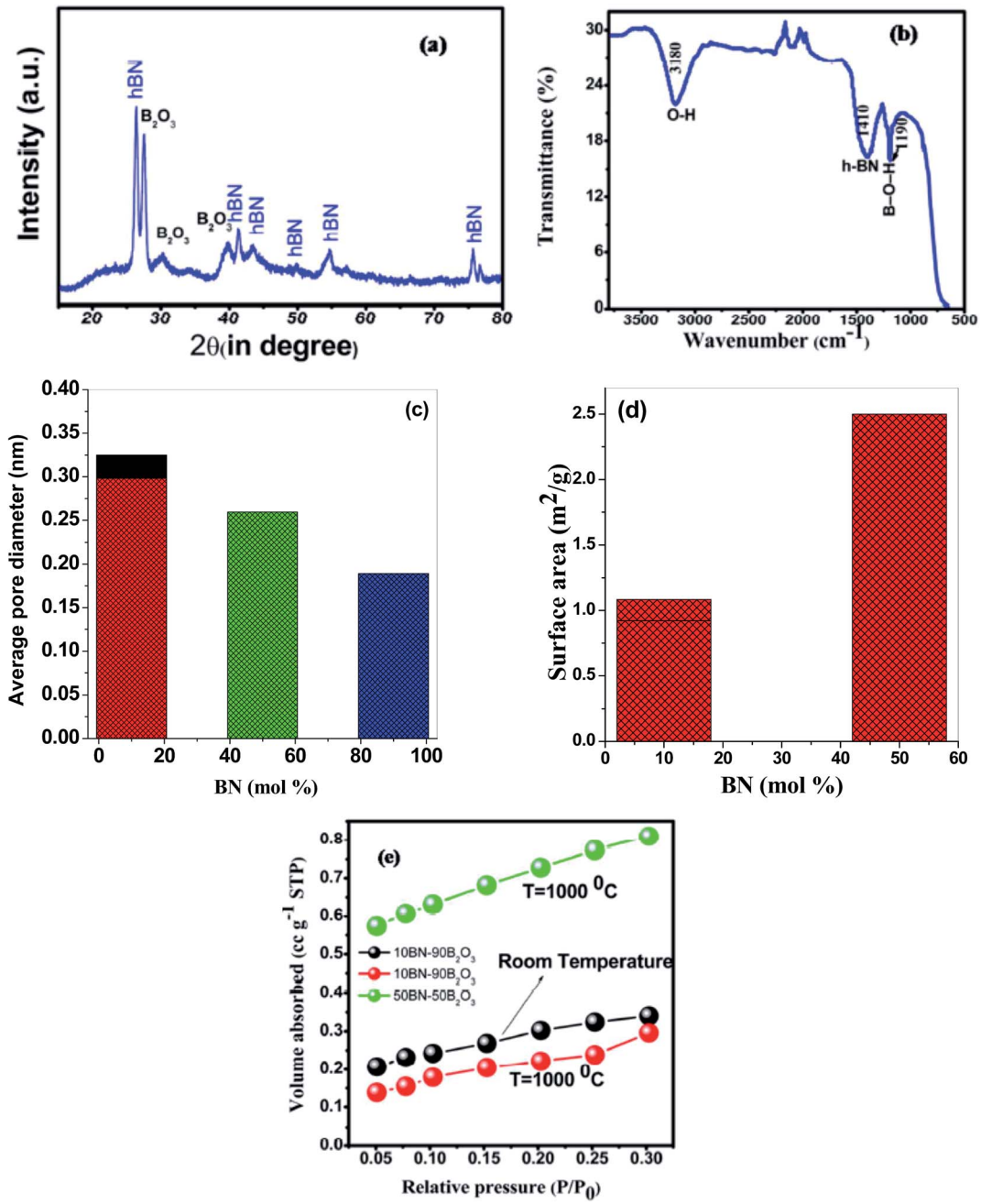

Fig. 1 Characterizations of porous h-BN architecture of (a) XRD showing the formation of h-BN phase (b) FTIR spectra of showing different types of the bonds as marked by their corresponding wave numbers (c) variation of average pore diameter *vs.* h-BN content (d) the bar graphs of surface area with increasing % of h-BN and (e) variation of volume absorbed with relative pressure of different samples sintered at 1000 °C.

Table 1 Compositions, contact angle, BET surface area and BET average pore size diameter and grain size sintered at 1000 °C

Compositions	Contact angle (°) at RT °C	BET surface area ($m^2\ g^{-1}m^{-1}$)	BET average pore size diameter (nm)	Calculated grain size (nm)
h-BN	69	—	—	638
10BN-90B_2O_3	28.98	1.084	0.325	—
10BN-90B_2O_3	—	0.922	0.298	789
50BN-50B_2O_3	52	2.500	0.259	1100
90BN-10B_2O_3	45	—	0.189	1125

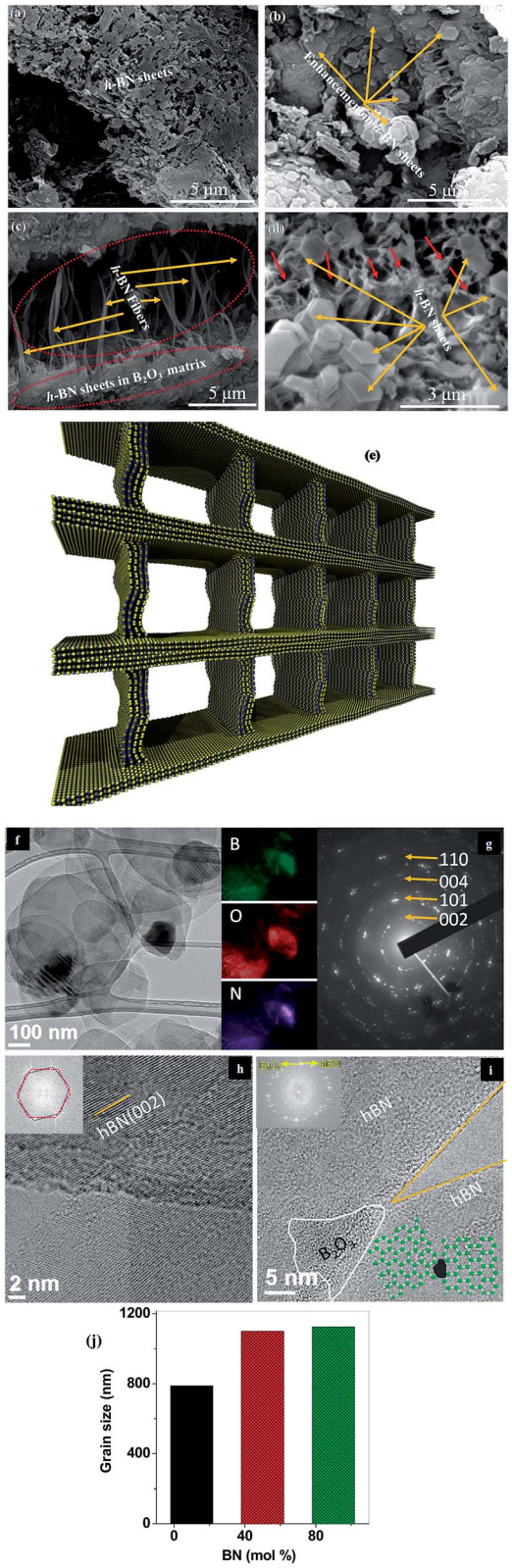

Fig. 2 Surface morphology of porous h-BN and grain size distributions (a) h-BN SEM image revealing the tiny sheets of h-BN and are interconnected to each other. (b and c) Low – magnification SEM image of showing more interconnected h-BN big sheets (d) high – magnification SEM image of 50BN-50B_2O_3 shows the fully developed pores with h-BN interconnected stacked sheets. Nanostructures of porous h-BN (e) schematic of 3D architecture of hBN (f) low magnification bright field TEM image showing large h-BN sheet with porosity. Inset showing EELS map of B and N of the sheet (g) the selected area electron diffraction (SAED) showing hexagonal pattern of h-BN (h) high magnification image at the edge of the sheet showing the number of layers of BN across to the (002) plane in these large size sheets (i) typical TEM image of the synthesized h-BN nanosheets, resulting in geometrically defined edges (j) variation of grain size *vs.* BN content.

confirm that 3D BN architecture includes the hierarchical porous structure in comparison to BN nanosheets. It also includes macroporosity between the sheets (100–200 nm diameter) and microporosity (1–2 nm) within the single nanosheet. The energy filter composition map shows the chemical composition of the 2D sheets which are made of B, O and N (Fig. 2f). The insert SAED pattern shows four characteristics diffraction rings that correspond to (002), (101), (004) and (110) lattice planes of h-BN respectively. These observations are well consistent with the XRD results (Fig. 2g). Besides the SAED pattern, HRTEM image (Fig. 2h) reveals a layered h-BN structure with an interlayer distance of 0.34 nm (Fig. 2i) corresponding to the inter-plane distance (002) in agreement with reported values. High-resolution HRTEM image shows that the atoms are uniformly arranged in a hexagonal symmetry.[45] It is well known that if grain size is increasing then the voids among them will also be increases and therefore the pore size is also increasing with increasing h-BN concentration. The calculated values of grain size from the SEM images lies in the range from 789–1125 nm. It is observed form the plot of grain size *vs.* BN mol% that the grain size increases with increasing the doping concentration of h-BN (Fig. 2j).

3.5. Mechanical behaviour

For the mechanical test of the porous 3D architecture, the sample was compressed by Instron universal testing machine. The compressive load–displacement curve exhibited a high load bearing capacity of the order of ~2.9 kN (Fig. 3a). The calculated values of ultimate stress are found to be ~37 ± 5 MPa which is higher than previously reported values.[46] The high load bearing capacity of the 3D structure is shown in Fig. 3a inset (under the curve). The standard densities of boron nitride and boron trioxide are 2.1 and 2.4 g cm^{-3} respectively. However, the value of the density of synthesized porous h-BN was 1.3 g cm^{-3} (Fig. 3b). The SEM images of the compressed samples were also examined to verify the 3D porous structure behaviour after the loading procedure. The images revealed that the h-BN sheets arrest the crack propagations. The yellow colour arrows in Fig. 3c and d highlighted the interlocking of h-BN sheets in the formed cracks. Fig. 3c displayed how the h-BN sheets are distributed and the cracked area has been covered by them. These sheets prevent the crack propagation as well as divert the path of the crack propagation, which is represented by the yellow color lines (Fig. 3d). To understand the porosity of the synthesized h-BN, contact angle measurements were also carried out. It was observed that porous h-BN samples show hydrophilicity (contact angle range from 52–75°) (Fig. S4 ESI†). This study

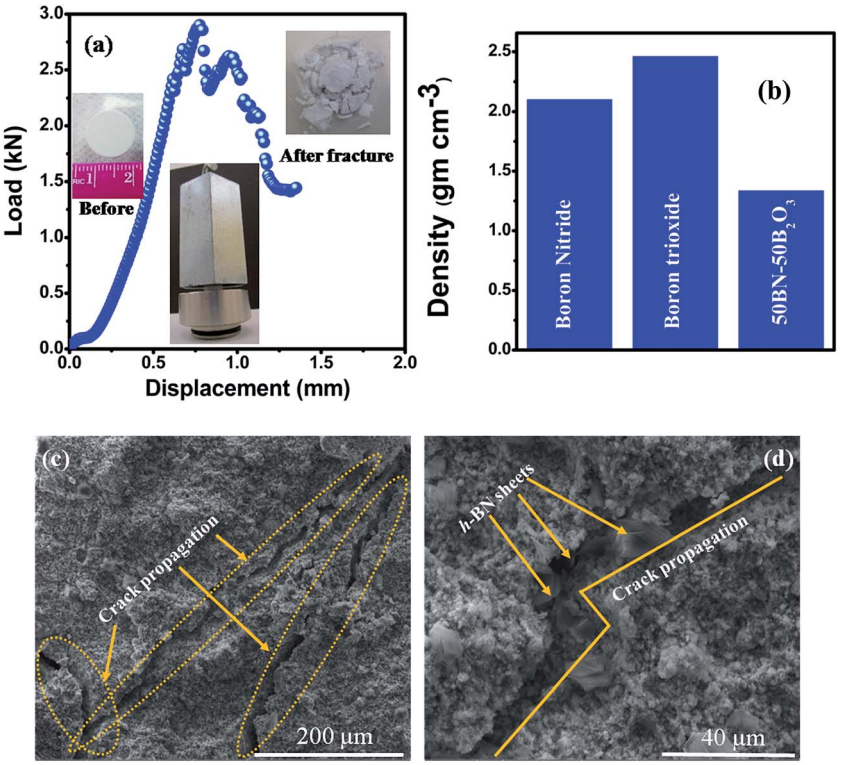

Fig. 3 Mechanical characterizations of the porous h-BN. (a) Variation of load *vs.* displacement. The inset shows the pellet samples view before the test and after fracture test. (b) Comparison of density with standard density of boron nitride, boron trioxide, porous h-BN. The bar graphs of density reveal that h-BN density was low 1.33 gm cm^{-3}(c) low magnification SEM image of fractured sample revealing the h-BN sheets are interlocking the crack propagation, (d) at high magnification SEM image showing the crack divergence due to h-BN sheets.

confirms the porous nature of the samples on the surface as well as inside of the samples.

3.6. Molecular dynamics simulations analysis

To investigate whether humidity affects the h-BN sheet network, mechanical properties, we carried out molecular dynamics (MD) simulations. We employed the Reactive Force Field (ReaxFF)[47] in the LAMMPS MD package[48] implementation,[49] which is capable of describing bond breakage/formation. We used a chain of three Nosé-Hoover thermostats to carry out simulations in the NVT ensemble, and the resulting equations of motion were subject to integration with a time-step of 0.1 femto seconds. The structures we tested are presented in Fig. 4a and b. The system is periodic in the plane of the 8.57 nm per 8.54 nm h-BN tri-layers, and non-periodic in the other direction. The four layered sheet is 7.8 nm high. In our tests we: (a) minimized the structure; (b) generated an ensemble of velocities corresponding to a temperature of 300 K; (c) increased the downward stress on the top trilayer by 0.48 MPa per picoseconds (ps); (d) performed an equilibration for 120 000 time-steps once pressure reached 2.4 MPa; (e) resumed the 0.48 MPa ps^{-1} stress increase until failure. The edges of the bottom trilayer were also kept fixed, except during minimization. Fig. 4e presents results for tests with an absolute humidity of 0 and 2.9 g L^{-1}. For the case without humidity, failure started when the applied stress reached 48 MPa. This is rather low, considering the in-plane Young's modulus of monolayer h-BN is greater than 1 TPa.[50] However, h-BN resistance to out-of-plane deformations is not as high. For instance, the stiffness tensor component C33 of a bulk sample is only 32 GPa.[51] In our tests, failure was due to out-of-plane bending of the vertical h-BN sheet, see Fig. 4c. The yield strength observed in simulation closely matches with our experimental observations. For the case with humidity, failure started when the compressive stress reached a slightly lower value, 36 MPa. The failure here was again related to bending of the vertical h-BN sheet, see Fig. 4d. While humidity greatly changed resistance, it influences on failure stress was not as large. Our MD simulations indicate that the h-BN sheet network would retain good mechanical properties if used in humidity sensors. Note also that the considered humidity value is rather high; typical absolute humidity values fall in the 0.01 g L^{-1} range.

3.7. LPG and humidity sensing behaviour

The LPG and humidity sensing investigations of the 3D architecture were also carried out using their thin film samples. The variations in electrical resistance as a functional of time for different concentrations of LPG are shown in Fig. 5a. It is observed from the both curves that the resistance of the film sample increases with increasing time and thereafter it becomes saturated. Further, the resistance diminishes

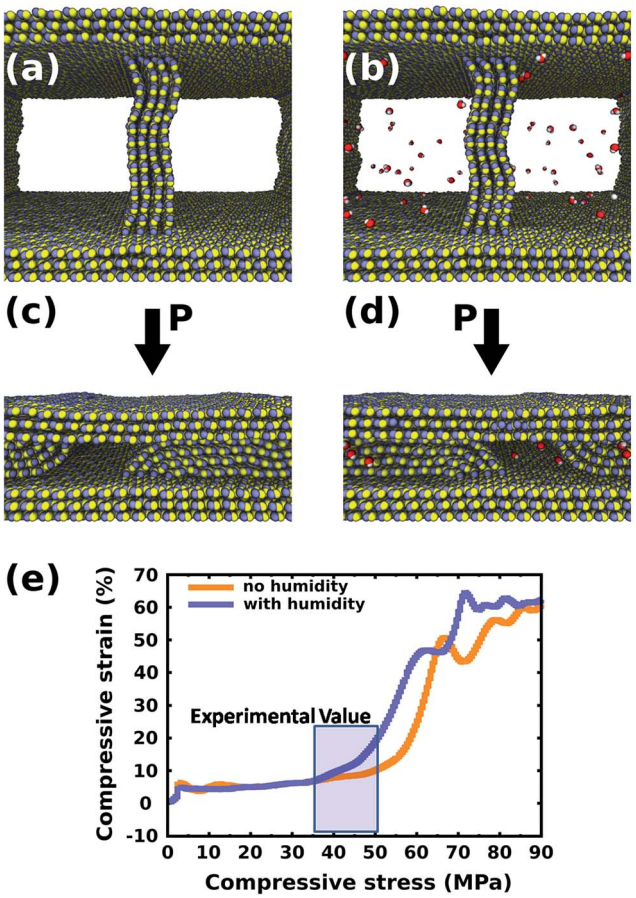

Fig. 4 Structures used to perform molecular dynamics compression tests. (a) and (c) Present snapshots before and after failure for the case without humidity, while (b) and (d) present snapshots for the case with humidity. Increasing stress was applied to the top horizontal trilayer, and the resulting strain was measured. The results, presented in (e), show a small decrease in the 3D architecture strength due to humidity presence, the yield strength matches with experimental observations.

drastically in opened outlet condition and attains the stabilized resistance value. The calculated values of the sensitivity and sensor response were found 0.14 and 6.17 along with a response and recovery times of ~55 and 40 s respectively. These measurements were again repeated after two months which are plotted and showed in the inset of Fig. 5a. No significant changes were observed which confirmed the stability of the sensor. Fig. 5b shows that the humidity sensing characteristics of the porous h-BN film with change in % RH. In the lower humidity range (10–40%RH) the resistance decreases whereas at higher humidity range (40–90% RH) shows a decrement. The calculated sensitivity of the sensor is 1.47 MΩ/% RH and 0.29 MΩ/%RH for low and high humidity range respectively. Fig. 5b inset shows the reproducibility the same variation after two months which represent the stability of the sensor. The sensing properties of the h-BN nanosheets gas sensor upon exposure to air, chemisorptions of the oxygen and also captured the electron from the adsorption sites on the surface. The electron extracted from the conduction band increases the resistance. The interaction of oxygen ions on the surface of h-BN modified the electron transport in the film. The details of such sensing properties were reported in the literature.[52–54] Similarly, the h-BN sensor upon exposure to LPG, reaction due to the ejection of the electrons (charge carriers), the resistance of the film. A schematic explaining the mechanism is illustrated through Fig. 5c. The process of chemisorptions occurs at very low humidity level and remains unaltered by further changes in humidity.

A schematic diagram shows the whole mechanism and is shown in Fig. 5d. When the h-BN nanosheets gas sensor is exposed to air, oxygen gets chemisorbed on the surface of the sample and arrest electron from the adsorption sites on the surface which depends on the temperature forms either, O_2^-, O^- or O^{2-}. For a sensor operating at room temperature, formation of O^{2-} is favoured. The associated reaction kinematics were represented as:[55]

$$O_2(gas) \leftrightarrow O_2(ads)$$

$$O_2(ads) + e^- \rightarrow O_2^-$$

This electron extraction from the conduction band tends to increase the resistance R, of the sensor. The adsorption of O_2^- ions of the nanostructured h-BN surface is necessary to increase the receptor activity of the sensor and also its sensing response. Oxygen vacancies may be the good position for the adsorption of oxygen on the surface of the sample and the subsequent formation of O_2^- depletion layer. Electron transfer from conduction band to the chemisorbed oxygen attributed to decrease of electron concentration on the film surface of the sample. Therefore, an increase in the value of R of h-BN film was observed. After a while, R, of the h-BN nanosheets got stabilized by the above chemisorption reactions mechanisms and was represented as stabilized resistance in the presence of air (R_a). When the h-BN sensor is introduce to LPG then it reacts with the chemisorbed oxygen and a surface charge layer was formed according to the reaction.[56]

$$C_nH_{2n+2} + O_2^- \rightarrow C_nH_{2n}O + H_2O + e^-$$

where, C_nH_{2n+2} represent hydrocarbons. Due to the ejection of the electrons as charge carriers, the resistance of the film decreases after its contact with the LPG. The depiction of the water adsorption process on the BN surface is illustrated in Fig. 5d. The hydroxyl groups, generated by the self-ionization of water molecules adsorbed on the activated surface of crystalline grain covers the surface area of h-BN through the chemisorption of water in moist surroundings. The process of chemisorption occurs at very low humidity level and remains unaltered by further changes in humidity. Humidity gets adsorbed throughout the open pores leading to condensation within the capillary pores that are distributed among the grains of h-BN.[57] Therefore, the high porosity and

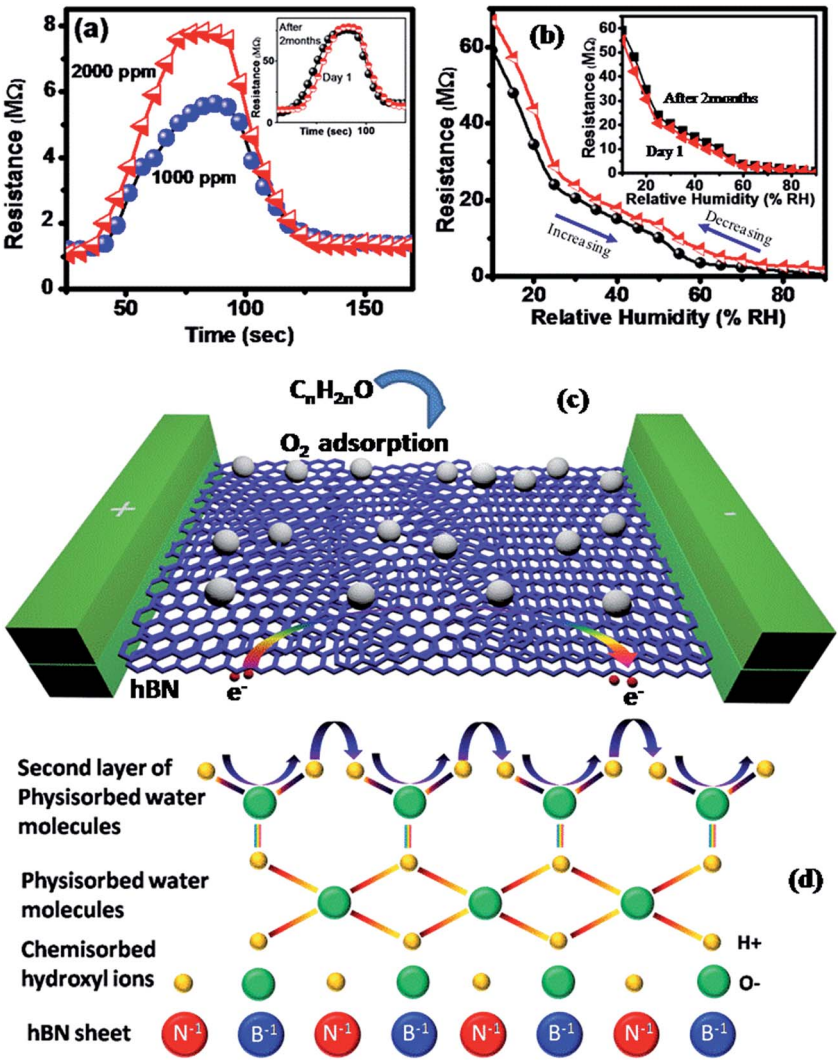

Fig. 5 LPG and humidity sensing characterization of the porous h-BN sensors. (a) Dynamic LPG sensing curves of 3D porous h-BN and inset showing stability curves of the LPG sensor. (b) Humidity sensing curves of the h-BN film and inset showing stability curves of the humidity sensor. Schematic diagram of (a) LPG sensing and (b) humidity sensing mechanism.

surface area are responsible to enhanced the sensitivity of the sensor.

4. Conclusions

In summary, we have demonstrated the synthesis of porous h-BN based nanosensors which can be used for the selective detection of humidity and LPG. This novel porous h-BN shows a very high sensitivity of the sensor is 1.47 MΩ/%RH and 0.29 MΩ/%RH for low (10–40% RH) and for high (40–90%RH) humidity respectively. The sensitivity of sensor retains till two months. The detecting method of humidity and LPG, this study is the first to integrate the h-BN performance in the form of nanosensor. The experimental and simulation study clearly reveals the porous high surface area 3D architecture retains its mechanical properties in humid environments as well. Considering its high selectivity, sensitivity, and simplicity, we believe that the innovative mechanism of porous h-BN will serve as the mile-stone for related studies and contribute to the future development in sensors technology.

Acknowledgements

The CRG (C. R. Gautam) acknowledge University Grants Commission, New Delhi, Government of India, for provided the Raman Fellowship for a year to carry out this work at Dept. of Materials Science and Nanoengineering (MSNE), Rice University, Houston Texas. The U.S. Air Force Office of Scientific Research (Award No. FA9550-14-1-0268 and Award No. FA9550-12-1-0035) also acknowledge for providing the financial support. S. J. acknowledges the Raman fellowship from UGC, Govt. of India. LDM and DSG acknowledge computational and financial support from the Center for Computational Engineering and Sciences at Unicamp through the FAPESP/CEPID

Grant No. 2013/08293-7. LDM acknowledges financial support from the Brazilian Federal Agency CAPES *via* its PNPD program.

References

1 C. Zhu, T. Y. J. Han, E. B. Duoss, A. M. Golobic, J. D. Kuntz, C. M. Spadaccini and M. A. Worsley, *Nat. Commun.*, 2015, **6**, 6962.
2 S. Vinod, C. S. Tiwary, P. A. S. Autreto, J. T. Tijerina, S. Ozden, A. C. Chipara, R. Vajtai, D. S. Galvao, T. N. Narayanan and P. M. Ajayan, *Nat. Commun.*, 2014, **5**, 4541.
3 B. Senyuk, N. Behabtu, A. Martinez, T. Lee, D. E. Tsentalovich, G. Ceriotti, J. M. Tour, M. Pasquali and I. I. Smalyukh, *Nat. Commun.*, 2015, **6**, 7157.
4 J. G. Alauzun, S. Ungureanu, N. Brun, S. l. Bernard, P. Miele, R. Backov and C. Sanchez, *J. Mater. Chem.*, 2011, **21**, 14025.
5 S. Schlienger, J. Alauzun, F. Michaux, L. Vidal, J. Parmen tier, C. Gervais, F. Babonneau, S. Bernard, P. Miele and J. B. Parra, *Chem. Mater.*, 2012, **24**, 88.
6 D. Liu, W. Lei, S. Qin and Y. Chen, *Sci. Rep.*, 2014, **4**, 4453.
7 J. Yin, X. Li, J. Zhou and W. Guo, *Nano Lett.*, 2013, **13**, 3232.
8 P. Kumbhakar, A. K. Kole, C. S. Tiwary, S. Biswas, S. Vinod, J. T. Tijerina, U. Chatterjee and P. M. Ajayan, *Adv. Opt. Mater.*, 2015, **3**, 828.
9 C. Y. Zhi, Y. Bando, C. C. Tang, H. Kuwahara and D. Golberg, *Adv. Mater.*, 2009, **21**, 2889.
10 A. Siria, P. Poncharal, A. L. Biance, R. Fulcrand, X. Blase, S. T. Purcell and L. Bocquet, *Nature*, 2013, **494**, 455.
11 F. Guinea, M. Katsnelson and A. Geim, *Nat. Phys.*, 2009, **6**, 30.
12 D. Liu, W. Lei, S. Qin, K. D. Klikab and Y. Chen, *Phys. Chem. Chem. Phys.*, 2016, **18**, 84.
13 D. Liu, L. He, W. Lei, K. D. Klika, L. Kong and Y. Chen, *Adv. Mater. Interfaces*, 2015, **2**, 1500228.
14 P. Mulpur, S. Yadavilli, A. M. Rao, V. Kamisetti and R. Podila, *ACS Sens.*, 2016, **1**(6), 826.
15 D. Liu, W. Lei, S. Qin, K. D. Klika and Y. Chen, *Phys. Chem. Chem. Phys.*, 2016, **18**, 84.
16 M. Neek-Amal, J. Beheshtian, A. Sadeghi, K. H. Michel and F. M. Peeters, *J. Phys. Chem. C*, 2013, **117**, 13261.
17 H. Yu, H. Kim, T. Kim, K. Bae, S. Seo, J. Kim, T. Kang and Y. Kim, *ACS Appl. Mater. Interfaces*, 2014, **6**(11), 8320.
18 B. M. Kulwicki, *J. Am. Ceram. Soc.*, 1991, **74**, 697.
19 E. Traversa, *Sens. Actuators, B*, 1995, **23**, 135.
20 N. Yamazoe and Y. Shimizu, *Sens. Actuators*, 1986, **10**, 379.
21 A. Buvailo, Y. Xing, J. Hines, N. Dollahon and E. Borguet, *ACS Appl. Mater. Interfaces*, 2011, **3**(2), 528.
22 Y. Sakai, M. Matsuguchi and Y. Sadaoka, *Sens. Actuators, B*, 1996, **35**, 85.
23 Y. Sakai, M. Matsuguchi and N. Yonesato, *Electrochim. Acta*, 2001, **46**, 1509.
24 M. J. Yang, Y. Li, N. Camaioni, G. C. Miceli, A. Martelli and G. Ridolfi, *Sens. Actuators, B*, 2002, **86**, 229.
25 M. J. Yang, G. C. Miceli, N. Camaioni, C. M. Mari, Y. Li and M. Ling, *J. Appl. Electrochem.*, 2000, **30**, 753.
26 H. Aoki, H. Shima, C. Kimura and T. Sugino, *Diamond Relat. Mater.*, 2007, **16**, 1300.
27 Y. Yu, H. Chen, Y. Liu, L. H. Li and Y. Chen, *Electrochem. Commun.*, 2013, **30**, 29.
28 A. Soltani, P. Thevenin, H. Bakhtiar and A. Bath, *Thin Solid Films*, 2005, **471**, 277.
29 S. Singh, B. C. Yadav, M. Singh and R. Kothari, *Int. J. Sci. Tech. Soc.*, 2015, **1**, 6.
30 X. Zhou, Q. Cao, Y. Hu, J. Gao and Y. Xu, *Sens. Actuators, B*, 2001, **77**, 443.
31 X. Zhou, Q. Cao, H. Huang, P. Yang and Y. Hu, *Mater. Sci. Eng., B*, 2003, **99**, 44.
32 A. Teleki, S. E. Pratsinis, K. K. Sundaram and P. I. Gouma, *Sens. Actuators, B*, 2006, **119**, 683.
33 S. Z. Butler, S. M. Hollen, L. Cao, Y. Cui, J. A. Gupta, H. R. Gutiérrez, T. F. Heinz, S. S. Hong, J. Huang, *et al.*, *ACS Nano*, 2013, **7**(4), 2898.
34 W. J. Liu, T. T. Qian and H. Jiang, *Chem. Eng. J.*, 2014, **236**, 448.
35 T. Hyodo, Y. Yuzuriha, O. Nakagoe, T. Sasahara, S. Tanabe and Y. Shimizu, *Sens. Actuators, B*, 2014, **202**, 748.
36 D. Ghosh, B. Ghosh, S. Hussain, S. Chaudhuri, R. Bhar and A. K. Pal, *Appl. Surf. Sci.*, 2012, **263**, 788.
37 B. C. Yadav, R. Singh and S. Singh, *J. Exp. Nanosci.*, 2013, **8**, 670.
38 C. C. Tang, Y. Bando, Y. Huang, C. Zhi and D. Golberg, *Adv. Funct. Mater.*, 2008, **18**, 3653.
39 W. W. Lei, D. Portehault, D. Liu, S. Qin and Y. Chen, *Nat. Commun.*, 2013, **4**, 1777.
40 W. W. Lei, D. Portehault, R. Dimova and M. Antonietti, *J. Am. Chem. Soc.*, 2011, **133**, 7121.
41 C. Devallencourt, J. M. Saiter, A. Fafet and E. Ubrich, *Thermochim. Acta*, 1995, **259**, 143.
42 Y. Liu, Y. Wang, S. Zhou, S. Lou, L. Yuan, T. Gao, X. Wu, X. Shi and K. Wang, *ACS Appl. Mater. Interfaces*, 2012, **4**, 4913.
43 R. Ma, Y. Bando and T. Sato, *Chem. Phys. Lett.*, 2001, **337**, 61.
44 C. Jin, F. Lin, K. Suenaga and S. Iijima, *Phys. Rev. Lett.*, 2009, **102**, 195505.
45 C. Zhi, Y. Bando, C. Tang, D. Golberg, R. Xie and T. Sekigushi, *Appl. Phys. Lett.*, 2005, **86**, 213110.
46 M. A. Rafiee, T. N. Narayanan, D. P. Hashim, N. Sakhavand, R. Shahsavari, R. Vajtai, P. Ajayan and M. Ajayan, *Adv. Funct. Mater.*, 2013, **23**, 5624.
47 A. C. T. van Duin, S. Dasgupta, F. Lorant and W. A. Goddard, *J. Phys. Chem. A*, 2001, **105**, 9396.
48 S. Plimpton, *J. Comput. Phys.*, 1995, **117**, 1.
49 H. M. Aktulga, J. C. Fogarty, S. A. Pandit and A. Y. Grama, *Parallel Comput.*, 2012, **38**, 245.
50 S. M. Kim, A. Hsu, M. H. Park, S. H. Chae, S. J. Yun, J. S. Lee, D. H. Cho, W. Fang, C. Lee, T. Palacios, M. Dresselhaus, K. K. Kim, Y. H. Lee, J. Kong, *et al.*, *Nat. Commun.*, 2015, **6**, 8662.
51 J. F. Green, T. K. Bolland and J. W. Bolland, *J. Chem. Phys.*, 1976, **64**, 656.
52 K. K. Dey, D. Bhatnagar, A. K. Srivastava, M. Wan, S. Singh, R. R. Yadav, B. C. Yadav and M. Deepa, *Nanoscale*, 2015, **7**, 6159.

53 S. Singh, A. Singh, B. C. Yadav, P. Tandon, S. Kumar, R. R. Yadav, S. I. Pomogailo, G. I. Dzhardimalieva and A. D. Pomogailo, *Sens. Actuators, B*, 2015, **207**, 460.
54 R. K. Sonker, S. R. Sabhajeet, S. Singh and B. C. Yadav, *Mater. Lett.*, 2015, **152**, 189.
55 C. C. Hsiao and L. S. Luo, *Sensors*, 2014, **14**, 12219.
56 S. Choopun, N. Hongsith and E. Wongrat, in *Nanowires Recent advances*, ed. X. Peng, Intech Open, Telegraph Way, Winchester, UK, 2012, DOI: 10.5772/54385.
57 M. Singh and B. C. Yadav, *Sens. Transducers J.*, 2015, **186**, 140.